IEEE Robotics and Automation Letters (RA-L) paper, presented at ICRA 2026, Vienna, Austria. Cite as RA-L paper.

Anti-Backlash Mechanisms for Cycloidal Drive Robotic Actuators: Design and Evaluation

Wesley Roozing[1] and Jelmer Volbeda

***Abstract*— We design and experimentally evaluate two anti-backlash mechanisms for cycloidal reducers. The two mechanisms are integrated into variations of a proposed design of quasi-direct drive actuator. Three prototypes are realised to compare the two mechanisms against the baseline design. We evaluate the effectiveness of the anti-backlash mechanisms under varying preload with measurements of friction, backlash, and stiffness. The results demonstrate that the anti-backlash mechanisms are effective at reducing backlash by approx. 2-3x, at the expected expense of increased friction (<2x).**

I. Introduction

Recent interest in highly dynamic (legged) robots has consequently increased the interest in dynamically capable, power-dense actuator technology. Many of these robots use quasi-direct drive (QDD) actuators [1], with low reflected inertia, current-based torque control, increased efficiency, shock absorption, and high peak speeds.

Most QDD actuator designs use planetary gears (e.g., [2]–[8]). Although an efficient and mature technology, these reducers, as well as their variants (e.g., wolfrom) have small feature sizes (e.g., gear teeth) that require tight tolerances. Furthermore, their torque transmission relies on the shear strength of the teeth, which negatively affects torque capacity and robustness [9], [10]. In comparison, cycloidal reducers have larger features for similar reduction ratios and sizes, and rely on compressive forces for torque transmission. As a result, they can offer important benefits, including torque capacity, torsional stiffness, and physical (impact) robustness. We and other authors have recently developed several lightweight and compact cycloidal drive actuators [11]–[16]. In particular, these works demonstrated high efficiency at low torques in addition to the benefits stated above.

At low reduction ratios, the larger feature sizes of cycloidal drive geometry also makes them well suited for low-cost (larger tolerance) manufacturing including 3D printing, aiding rapid customisation for different requirements. We explored low-reduction 3D printed cycloidal drives in our previous works [11], [12], with promising results. Recently other authors have also started to explore 3D printed planetary and cycloidal designs [9], [10], [17], [18].

Backlash is present in all high-efficiency transmission mechanisms, including planetary gears and cycloidal drives. Although some backlash is typically acceptable in the context of dynamic (legged) robots, the resulting inaccuracy compounds along joints in a series mechanism (e.g., limbs) and complicates control. This can be addressed using anti-backlash mechanisms, however, only a few examples exist for compact robotic actuators [19]–[23].

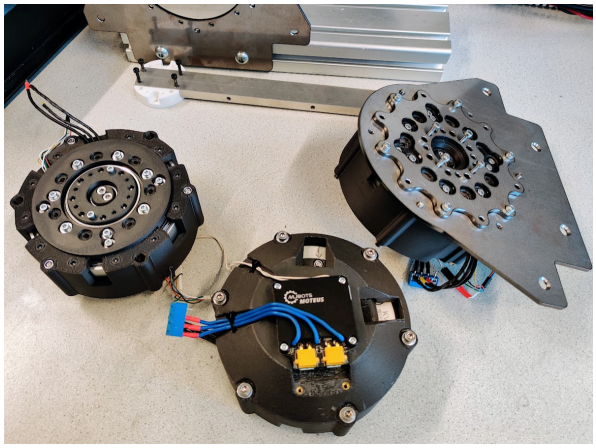

Fig. 1: Three prototypes: Output side (left), back side with controller (middle), and mounting with output locking plate (right).

The goal of this work is to design and evaluate anti-backlash mechanisms for compact, cost-effective, and high-power QDD actuators for legged robots. First, we present a cost-effective baseline actuator design with motor-embedded cycloidal gearing, increasing compactness. To our knowledge, the very recent work [14] is the only other work to design motor-embedded cycloidal gearing. Then, two anti-backlash mechanisms are developed and integrated into the design. To our knowledge, the only work to integrate an anti-backlash mechanism into a cycloidal reducer is [21], leveraging a conic cycloidal disk. The authors report positive results but significant details about the mechanism and design parameters are missing. We intend to provide more insight. We summarise the main contributions as follows:

1) A cost-effective QDD actuator design with a motor-embedded non-pinwheel cycloidal reducer, based on 3D printed and off-the-shelf components;
2) Two novel anti-backlash mechanisms for cycloidal reducers with adjustable preloading, incorporated into variations of the designed actuator;
3) Experimental validation of the effect of preload in both anti-backlash mechanisms against the baseline prototype, using three prototypes (Fig. 1).

This paper is outlined as follows. Sec. II describes the basic design concepts and relation to existing works. Sec. III describes the requirements, the proposed baseline design, and anti-backlash mechanisms. Sec. IV presents experimental results. Finally, Sec. V and VI conclude the work.

[1]Robotics & Mechatronics (RaM), Robotics Centre, University of Twente, The Netherlands. E-mail: w.roozing at utwente.nl.

TABLE I: Specifications of various QDD actuators.

	Proposed design	**Roozing et al. [11], [12]**	**Lee et al. [13]**	**Singh et al. [7]**	**PULSE 115-60 [6]**	**Yu et al. [8]**	**MIT Mini Cheetah [3]**	**ARTEMIS hip pitch [5]**	**ARTEMIS hip yaw [5]**	**Unitree GO-M8010-6 [24]**	**H. Zhu et al. [4]**	**A. Zhu et al. [14]**
Intended application	Humanoid	Legged robots	Legged robots	Quadruped	Dynamic robots	Hip exo.	Quadruped	Humanoid	Humanoid	Quadruped	Knee exo.	Legged robots
Peak speed (rpm)	120 (45V)	267‡ (40V)	177 (80V)	355‡ (48V)	90 (48V)	188 (42V)	382 (24V)	220 (44V)	239 (44V)	286 (24V)	154	129 (24V)
Nominal torque (Nm)	52 (20A)	36.4 (40A)	unknown	26.4	18.5 (3.6A)	17.5 (7.5A)	6.9	80	30	unknown	13	37.5
Peak torque (Nm)	156 (62A)	36.4 (40A)	150 (40A)	55.2	62.5 (14A)	42 (17A)	17	250	85	23.7 (40A)	unknown	90‡
Diameter (mm)	125	104	90	126	114	110	96	200*	100*	97	246*	156*
Height (mm)	62	58	37	68	64	52	40	60*	80*	42	68*	63*
Mass (kg)	1.35	0.797	1.85	1.89	1.25	0.77	0.440	3.00	0.850	0.53	1.15	1.40
Peak torque density (Nm/kg)	116	45.7	81.1	29.2	50.0	54.5	38.6	83.3	100	44.7	unknown	64.2‡
Power density (W/kg)	1452	1755	1507	1086†	471 (188†‡)	1074	1545 (568†)	1916	2500	1342	unknown	865
Reducer type	Cycloidal	Cycloidal	Cycloidal	Planetary	Planetary	Planetary	Planetary	Planetary	Planetary	unknown	Planetary	Cycloidal
Reduction ratio	13	11	11	8	5	8	6	5.9	14.5	6.33	7	10
Backlash (deg)	Sec. IV	0.3	unknown	unknown	0.2	unknown	0.3	unknown	unknown	unknown	unknown	0.12

*Estimated values.
†Positive power density as reported by authors. Other values are computed using peak torque and speed values (not achievable simultaneously).
‡Experimentally measured, i.e. accounting for resistive and frictional losses.

II. Design Concepts

A. Pinwheel and non-pinwheel cycloidal drives

Fig. 2 shows the principle geometry of a cycloidal reducer. Its main feature is the cycloidal disk (shown in green), which rolls around the non-pinwheel (in yellow) of pitch radius R and with N (12 in Fig. 2) lobes. Conversely, the disk typically has $N-1$ lobes, leading to a reduction ratio of $n = N - 1$. The cycloidal disk is driven by an input shaft with an eccentric cam (in blue), with eccentricity E. To transfer the rolling motion of the cycloid disk to a pure rotation of the output shaft, it has output holes of radius R_{oh} which interact with output pins (of radius R_{o}, in grey) on the reducer output shaft. We refer to the video attachment for a moving example.

The example shown in Fig. 2 is that of a *non-pinwheel* cycloidal drive [25], in which the non-pinwheel replaces a conventional *pinwheel* with pins or rollers (with radius R_{r}, shown as dashed red circles), with a profile optimised for meshing. This reduces its complexity and size while offering comparable performance characteristics [26]. Recent works on compact cycloidal drive actuators use varying approaches, from pinwheels [11], [13], fused rollers [14] (using housing-fixed pins), to non-pinwheels [12], [15]. For an in-depth discussion and experimental comparison of pinwheel and non-pinwheel variants, we refer to our previous work [12].

The geometry shown in Fig. 2 can produce significant vibrations due to the translational movement of the disk. This is commonly solved by employing two disks with 180 degree phase difference [11], [12]. An alternative is to use a single disk with counterbalance [15], that has benefits in terms of compactness and number of parts.

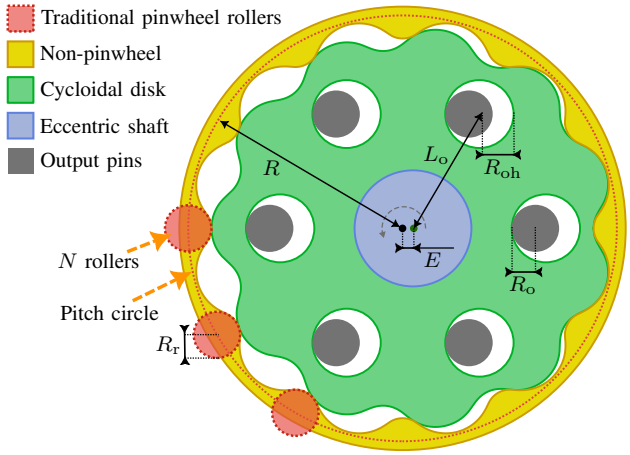

Fig. 2: Non-pinwheel cycloidal drive geometry.

B. Anti-backlash mechanisms

Concepts for anti-backlash mechanisms can be broadly classified into two categories; those employing parallel transmission paths [22], [23], [27], [28] and those employing direct preloading between meshing gears [19]–[21].

1) Parallel transmission paths: Anti-backlash mechanisms based on parallel transmission employ two gears meshing with one common gear, typically with one of the two being preloaded with a compliance, and classically with spur gears [27], [28]. This concept has recently been applied

to planetary reducers, with a modified planet carrier [22], and with a parallel rolling mechanism in [23].

2) Direct preloading of meshing gears: Contrary to parallel transmission paths, where preloading is in the driving direction, with direct preloading the compliance is typically perpendicular to the driving direction. This is commonly achieved by adding a preload spring in-line with the gear shaft and using conical or beveloid gears. [19], [20] apply this concept to 2K-V and planetary reducers, respectively, using beveloid gears. As described in Sec. I, to our knowledge, the only work to apply this concept to a (pinwheel) cycloidal reducer is [21], which utilises conical pins and cycloidal disk. The authors report positive results but information is limited.

Finally, we briefly note that some watches employ mechanically compliant gear teeth, combined with an oversized gear for preload. This is an interesting concept but is likely difficult to design for power transmission.

C. Quasi-direct drive (QDD) actuator design

The defining feature of QDD actuators is the combination of low gear ratios with high torque motors. Owing to the linear scaling of torque capacity and quadratic scaling of reflected inertia with reduction ratio, this achieves the benefits that have made QDD actuators a popular method for highly dynamic actuation [2]. For high torque, outrunner motors with a large air gap radius are commonly utilised. In most recent designs, the remaining space inside the stator is used for *motor-embedded gearing*, reducing the axial length of the actuator [3]. The ARTEMIS biped [5] takes this concept to an extreme, with very large hip pitch actuators capable of 250 Nm peak torque using only 5.9 reduction ratio.

The very recent work [14] is to our knowledge the only work to design motor-embedded cycloidal gearing rather than planetary gearing. Their reducer design is similar in its main features to our previous work [12], for example in the shoulder screw output pins with stiffness ring, and has some differences in the bearing arrangement. Contrary to ours, their non-pinwheel is in fact a 'fused roller' type, where the profile is not optimised based on the meshing with the cycloid disk but simply replaces the classical pins of a pinwheel design. The design we present in this work does use a proper non-pinwheel design. Table I presents an overview of various recent QDD actuators, including those developed in this work.

III. Design and prototypes

A. Requirements

We set the design requirements based on 1) State-of-the-art QDD designs listed in Table I, and 2) Biomechanical data of human legs [29]. The latter analyses knee, hip, and ankle torques and velocities during jumping and sprinting. Peak knee values while running are 4 Nm/kg and 67 rpm (7.0 rad/s). Assuming the knee joint of a small humanoid of 35 kg, we set the following requirements:

- Nominal torque of $\geq$50 Nm, peak torque of $\geq$140 Nm, and peak speed of 120 rpm (12.6 rad/s) at 45 V. We note again that peak torque and speed values cannot be achieved simultaneously.
- Baseline QDD actuator design with motor-embedded cycloidal reducer, from low-cost 3D printed PA6-CF and off-the-shelf steel components.
- That design should be minimally modified (for fair comparison) into variants including one of two anti-backlash mechanisms.

B. Actuator (baseline) design

Fig. 3 shows cross-sections of the baseline design. The design consists of one main housing part and a cap (both shown in red), with diameter of 125 mm (excl. mounting) and thickness of 62 mm. The selected motor is a CubeMars RO100, a low-cost high torque frameless motor with 70 mm inner radius. The cycloidal reducer non-pinwheel (yellow) fits tightly inside the stator (grey) and both are mounted to the main housing, which also seats the main output bearing.

The reducer itself is designed with 13:1 reduction ratio, with geometric design parameters given in Table II. We employ a single 25 mm thick disk with counterweight integrated on the input shaft part (shown in blue) to maximise torque transfer contact area and provide more straightforward integration of anti-backlash mechanisms (Sec. III-C). The eccentric shaft itself is reinforced with a steel shaft liner, which also provides a raceway for a needle bearing for the cycloidal disk. Both the eccentric shaft and housing employ compression screws that reinforce the printed components.

The output structure consists of the output disk and stiffener parts (shown in aqua) connected by 8 embedded hardened steel pins, which have M3 threads exposed to the outside of the output disk for direct connection to the driven load. Each pin interacts with the cycloid disk through 3 small drawn-cup needle bearings to increase efficiency and torque capacity. Both the input and output structures are supported by bearings at both ends. Finally, a Moteus r4.11 motor controller is integrated on the housing cap, with its magnetic encoder positioned above a magnet on the input shaft.

C. Anti-backlash mechanisms

In the following we present two anti-backlash mechanisms for cycloidal reducers, as variations on the baseline design of Fig. 3 for fair and direct comparison. We refer to these as the *conic disk* and *split pinwheel* designs.

TABLE II: Geometric design parameters.

R	34 mm	Pitch circle radius
N	14	Number of non-pinwheel lobes
R_{r}	3.5 mm	Non-pinwheel lobe ('roller') radius
E	1.5 mm	Eccentricity
L_{o}	20 mm	Output hole location
R_{oh}	6.0 mm	Output hole radius
R_{o}	4.5 mm	Output pin radius

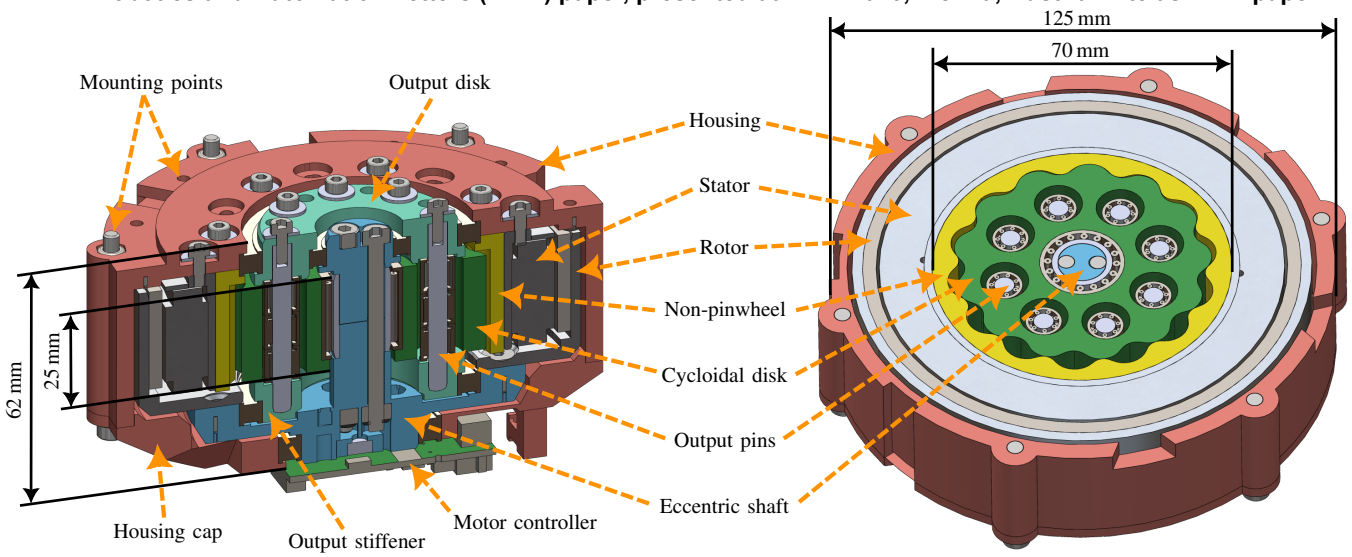

Fig. 3: CAD cross-section of the baseline design.

1) Conic disk: The concept of a conical cycloidal reducer assumes conical rollers on the pinwheel [21]. Applying this to a non-pinwheel cycloidal reducer such as here, both the cycloidal disk and non-pinwheel conical profiles can be generated by varying the roller radius linearly with the axial dimension of the reducer. The resulting profiles are connected using a lofting feature within the CAD software.

Fig. 4 shows the relevant components, including the adjustment mechanism. In this case the roller radius was varied $R_\mathrm{r} \in [3.1, 3.9]$ mm, which results in an inclination angle of $\theta = 3.5$ deg. With an adjustment range of $H = 3$ mm, this results in an adjustment range of 0.16 mm radially (assuming uniform offset). The preload and adjustment mechanism utilises two wave spring washers with two force distribution rings and adjustment screws for preload setting, allowing a preload of up to 54 N. As these parts are rotating relative to each other, a bearing is placed in between.

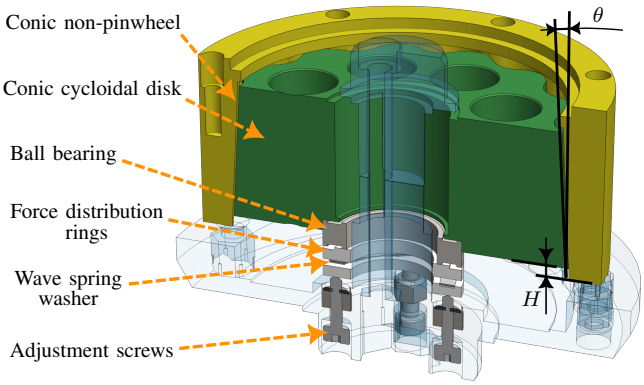

Fig. 4: Modified parts for the conic disk design.

2) Split pinwheel: The second anti-backlash mechanism relies on the principle of parallel transmission paths (Sec. II-B). The non-pinwheel is split into two stacked rings, one of which is rotationally offset around the axial direction and preloaded. The offset creates an effective widening of the lobes, reducing clearance with the cycloidal disk.

Fig. 5 shows the relevant components of this mechanism. Adjustment is achieved by sloped segments at the split of the rings, resulting in a screw-like motion. A slope angle of $\phi = 24$ deg and adjustment range of $H = 3$ mm creates up to a 2 deg offset between the rings axially. Screws with spring washers create the adjustment and preload. This anti-backlash mechanism has the largest effect at the edges of the non-pinwheel lobes, as these are the main contact points. The radius at these points is $r_\mathrm{c} = 31$ mm (Fig. 6). With 2 deg of rotation this results in a maximal adjustment of $r_\mathrm{c} \tan(\alpha) = 1.1$ mm near the lobes. At this configuration, the non-pinwheels compensate for a disk that is undersized by 0.37 mm. This configuration with such an undersized disk as example is shown in Fig. 6.

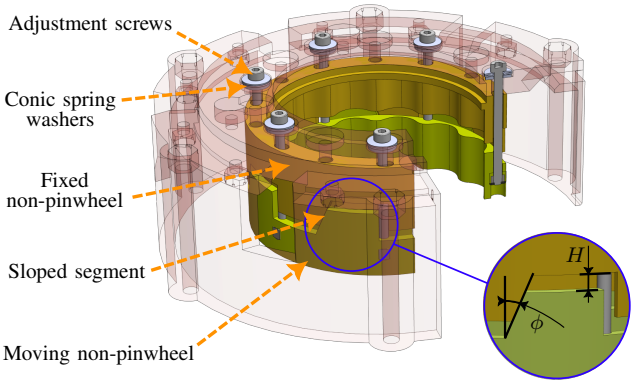

Fig. 5: Modified parts for the split pinwheel design.

D. Prototypes

Three prototypes were realised; a baseline, conic disk, and split pinwheel design, all shown in Fig. 1. The main components (baseline design) are shown in Fig. 7, partially assembled with bearings, locknuts, output pins, and shaft liner. The housing parts were manufactured from PC-CF

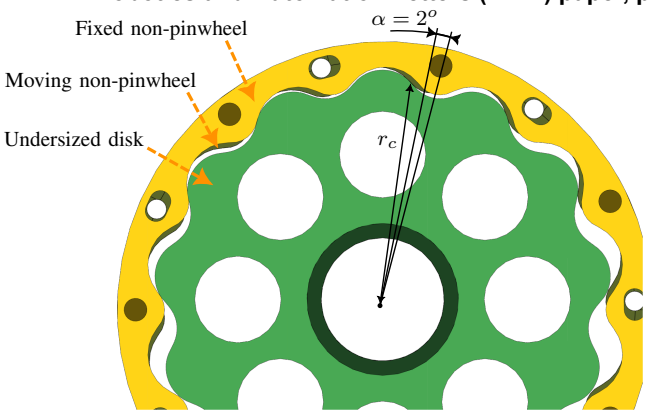

Fig. 6: Isometric top view of split pinwheel design showing meshing with an undersized disk.

(Prusament Polycarbonate Blend Carbon Fiber), a material that is exceptionally rigid and suitable for structural components. However, it is unsuitable for gearing parts, so these were manufactured from PA6-CF (MarkForged Onyx)[1]. The PC-CF parts were printed on a Bambu Labs X1 Carbon with 4 wall lines, 37% infill, and 0.2 mm layer height. The PA6-CF parts were printed on a Markforged Mark Two with 2 wall lines, 37% infill, and 0.2 mm layer height.

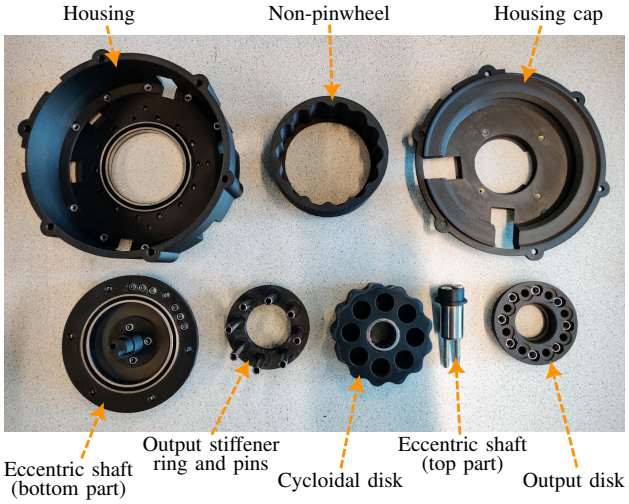

Fig. 7: 3D printed components of the baseline design.

The total mass of the actuators is 1.35 kg, of which 0.30 kg comprises printed parts. The total cost of the baseline design is approx. €300, as detailed in Table III. The variations including an anti-backlash mechanism cost approx. €6 more as they require additional springs and hardware.

IV. Experimental Results

The three prototypes were validated through a series of experiments, focusing primarily on the function of the anti-backlash mechanisms, followed by overall actuator testing in dynamic motions. During testing the actuators were rigidly mounted used steel fixtures from 3 mm sheet and controlled through the Moteus Python interface and a USB to CAN-FD interface device. Data was recorded at a rate of 100 to 400 Hz depending on the number of monitored variables. The design of all three prototypes and the testing code are fully open source, and available at [30].

A. Anti-backlash mechanism evaluation

1) Metrics and testing methodology: Evaluation of the anti-backlash mechanisms focuses on three performance metrics: friction, backlash, and stiffness. These metrics are measured for each actuator, before run-in, after run-in, and for 4 steps of preload increase for both anti-backlash mechanisms. The tests are performed as follows.

We estimate Coulomb friction in an unloaded configuration by slowly ramping the actuator output velocity between ± 13.2 rad/s over 120 s and taking its average value in both directions, estimated from current measurements.

We estimate backlash and stiffness by first locking the actuator output using an output locking plate (Fig. 1, right side). The actuator torque is then slowly increased in both directions to a specified maximum output torque (4 Nm in 4 s for backlash, 40 Nm in 20 s for stiffness). This is repeated 5 and 3 times, respectively, and the torque–deflection results averaged. However, backlash and stiffness are also expected to be dependent on the orientation of the output (and thus the cycloidal disk). To account for this, the tests are repeated at three different locked positions. These results are then again averaged, i.e., the final data is comprised of 15 and 9 experiments for backlash and stiffness, respectively, for each preload setting. The two resulting torque–deflection curves are used for estimation. Reducer backlash is estimated as the deflection difference at zero torque when approached from opposite sides. Stiffness is estimated from the slope in deflection when increasing torque, ignoring the initial backlash.

2) Run-in: Our previous work showed the importance of run-in of 3D printed cycloidal reducers [12]. All three actuators were run at 2.2 rad/s in alternating directions for 90 min. Torque reduced as expected, with all three actuators settling at a winding temperature of approx. 55 °C.

3) Main results: Using the previously described testing methodology, each actuator was tested before and after run-in. Subsequently the preload was increased in 4 steps from minimum to maximum for the two anti-backlash mechanisms, with testing at each step.

Fig. 8 shows the friction, backlash, and stiffness estimates over this series of experiments. As expected, all three reduc-

TABLE III: Bill-Of-Materials (BOM) of baseline actuator.

Frameless motor (CubeMars RO100)	€158
Motor controller (Moteus r4.11)	€72
Bearings & screws	€52
3D-printing filament	€18
Total	€300

[1]We verified that reducer parts of PC-CF resulted in excessive wear. A PC-PA (Taulman Alloy 910) material was also tested but this material showed a significant drop in stiffness at increasing temperatures.

ers show reduced friction after run-in, with increased backlash and slightly increased stiffness[2]. Interestingly, the conic disk design (in blue) shows the largest changes, particularly showing large backlash after run-in when the preload is still at minimum level. This suggests that this design needs a certain minimum preload to function.

Increasing the preload, both anti-backlash mechanisms show 1) increased friction, and 2) decreased backlash. This proves the principal effectiveness of the two approaches, and illustrates the trade-off that exists between the two when choosing preload. This trade-off is clearly shown by the Pareto front in Fig. 9. The two anti-backlash mechanisms are able to reduce backlash by approx. 2-3x, at the expensive of less than twice the friction, compared to baseline. In practice, the optimal preload level will depend on the specific application requirements, but it should be noted that both mechanisms reach a plateau where additional preload does not reduce backlash but does increase friction. Finally, while Fig. 9 suggest that overall the split pinwheel mechanism is the superior solution, we reiterate that it shows a significant reduction in stiffness as preload increases (Fig. 8).

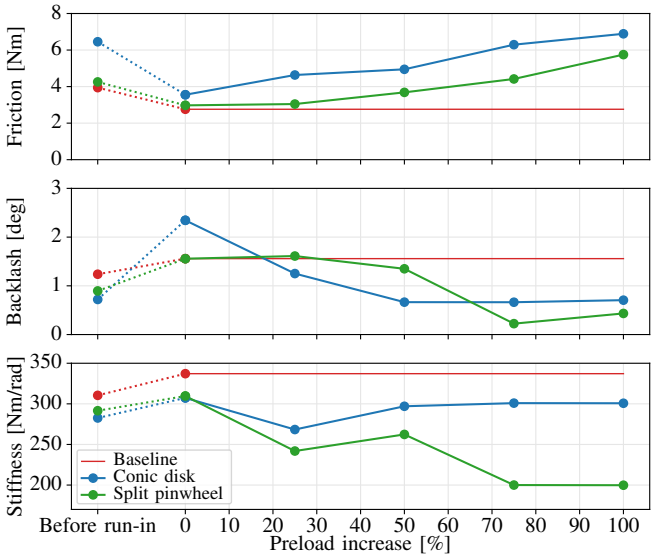

Fig. 8: Effect of preload on friction, backlash, and stiffness.

B. Dynamic motion performance

To assess overall actuator performance in dynamic applications, we perform a series of highly dynamic motions at increasing speed and acceleration. The load is a 0.3 m pendulum with plastic weights, weighing a total of 0.91 kg with inertia of 0.068 kg m^2. The setup is shown in Fig. 10. The motor controller uses a combination of regenerative braking and flux braking, which together with limited power sinking capability of the used power supply of our experimental setup necessitated a reduced supply voltage of 32 V to accommodate the most aggressive motions. At this voltage, the maximum achievable velocity is approx. 9 rad/s before voltage saturation. Therefore, the velocity limit for the built-in trajectory generation was set to 10 rad/s, in order to reach the limits of the system. Maximum acceleration and torque were set at 100 rad/s^2 and 100 Nm, respectively.

[2]We suspect that the stiffness increase, consistent across all three prototypes, is due to increased contact between the run-in parts.

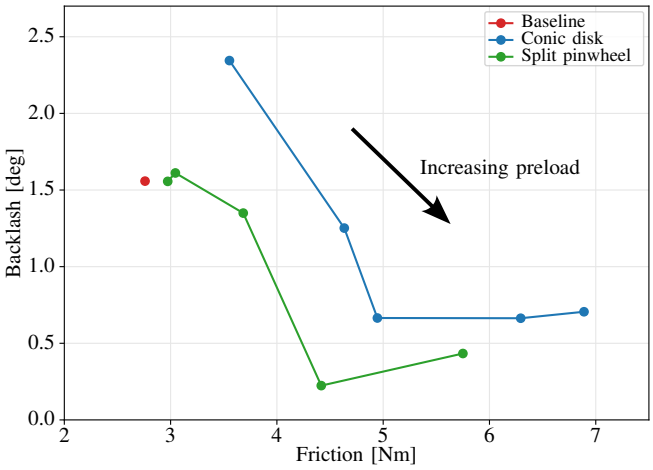

Fig. 9: Pareto front: Trade-off between backlash and friction.

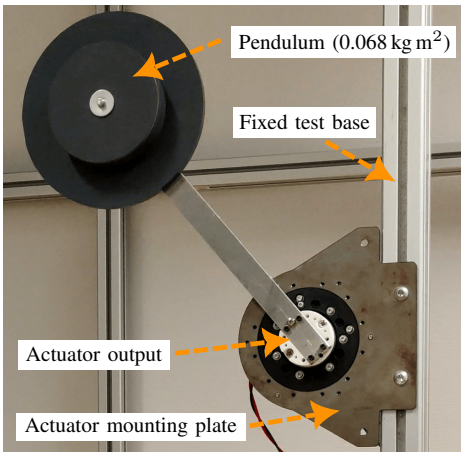

Fig. 10: Mounted actuator with pendulum for the motion control experiment (Sec. IV-B).

Fig. 11 shows the executed motion, with position, velocity and torque (from current) data. Fig. 12 shows the time periods around 12 and 31 s, with low (19 rad/s^2) and high (100 rad/s^2) accelerations, respectively. The actuator is able to robustly perform these highly aggressive motions combining high speeds and accelerations (torques). Notice that at peak velocities and at high accelerations up to 100 rad/s^2, the control torque limit of 100 Nm is quickly reached as voltage limits are reached and tracking errors increase. This can be observed at low torque and peak speed (Fig. 11 at 16 s), or at combined high speed and high torque (Fig. 12b). The system was also affected by limited stiffness of the test base (Fig. 10), as visible in the video attachment. Note that the *command* position was updated as soon as the *control* position reached it, resulting in larger position tracking errors overall. There are momentary peaks in torque (current) above 100 Nm that did not result in damage to the reducer, which

suggests that (momentarily at least) the reducer can provide significant torque. We also refer to the video attachment that shows these and other experiments.

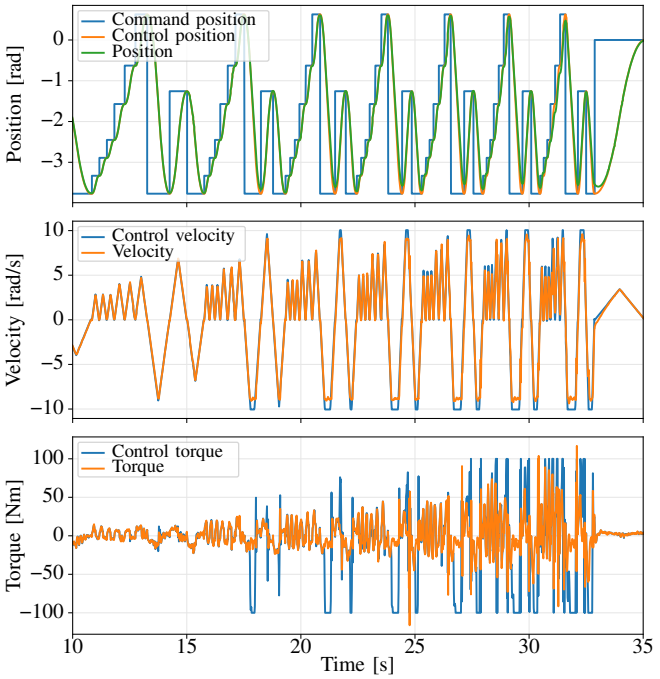

Fig. 11: Motion control: Position, velocity, and torque.

V. Discussion

We reflect on the results presented in Sec. IV in the context of the development of compact, cost-effective, high-power QDD actuators. First, the main results (Sec. IV-A) clearly demonstrate that the anti-backlash mechanisms are effective, producing the expected trade-off between reduced backlash at the cost of reduced efficiency. The current design is not fully optimized, as it was designed to accommodate three comparable prototypes. A more compact form factor can be achieved with individual optimisation. It should be pointed out that some level of backlash remains for both anti-backlash approaches. We attribute this to the fact that there are other backlash sources; in particular the tolerance between the output holes and output pins (observable backlash in the current prototypes). This warrants further investigation in the future. The non-planar geometry of the two anti-backlash mechanisms has important implications in the context of the layer lines of conventional FDM 3D printing. For the conic disk approach, this is clearly visible in the large increase of backlash and reduced friction after run-in, due to the sloped edges of both the cycloidal disk and non-pinwheel. Such issues will not occur when anti-backlash mechanisms are employed in CNC manufactured designs.

The dynamic motion results in Sec. IV-B showed that while the actuators are capable of highly dynamic and forceful motions, the current electronics are not sufficient to reach the limits of the actuator, instead being limited by voltage constrains and limited ability to sink negative electrical power on deceleration.

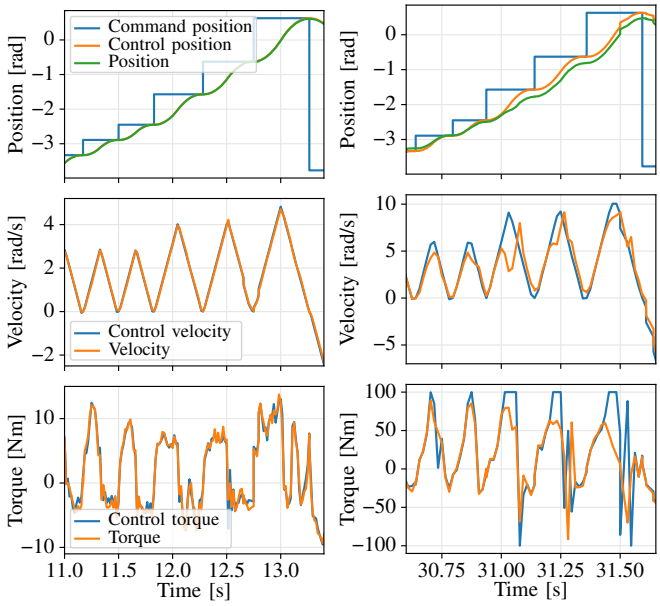

(a) Low acceleration (19 rad/s^2). **(b)** High acceleration (100 rad/s^2).

Fig. 12: Motion control: Close-ups of the data. Note the different time scales between the two columns.

Other testing of the three prototypes included peak torque and speed and impact testing, which showed promising results for this type of actuator design based on plastic cycloidal reducers. However, these current prototypes, when compared to our previous work [11], [12], exhibit relatively high friction and backlash, and low stiffness. In addition, sustained peak torque testing ($\gg$100 Nm) resulted in some plastic deformation of the cycloid disk. Hence, besides design changes, we stress the importance of the 3D printing and manufacturing process. Material selection and preparation, and printing settings, are critical in final reducer (and actuator) performance. These aspects were not fully optimised for these prototypes.

VI. Conclusions and Future Work

This work has focused on the development and evaluation of anti-backlash mechanisms for cycloidal reducers, in the context of compact, cost-effective, high-power QDD actuators. Two anti-backlash mechanisms were designed and integrated into variations of a baseline design. Both mechanisms were effective at reducing backlash, at the expected expense of increased friction. As discussed in Sec. V these first prototypes have some significant drawbacks but they provide an important proof of concept for anti-backlash mechanisms. Based on the results and our experience we believe that the conic disk approach is the more viable direction forward, due to its more straightforward implementation and the fact that it preserves regular meshing of the cycloid disk and non-pinwheel. It may be further refined to include anti-backlash for the output pins as well.

To push the envelope in actuator performance, we intend to continue improving the reducer design and overall packaging of cycloidal drive actuators. Suggested directions for future

work include use of low-cost CNC manufacturing for high-torque designs, mixed materials, axial flux motors, and integrated (liquid) cooling. For application in legged robots, designs should prioritise compactness and efficiency, and quantitative testing of endurance and impact robustness is suggested.

REFERENCES

[1] S. Seok *et al.*, "Design principles for energy-efficient legged locomotion and implementation on the MIT cheetah robot," *IEEE/ASME Transactions on Mechatronics*, vol. 20, no. 3, pp. 1117–1129, Jun. 2015.

[2] P. M. Wensing *et al.*, "Proprioceptive actuator design in the MIT cheetah: Impact mitigation and high-bandwidth physical interaction for dynamic legged robots," *IEEE Transactions on Robotics*, vol. 33, no. 3, pp. 509–522, Jun. 2017.

[3] B. Katz, J. D. Carlo, and S. Kim, "Mini cheetah: A platform for pushing the limits of dynamic quadruped control," in *2019 International Conference on Robotics and Automation (ICRA)*, May 2019, pp. 6295–6301.

[4] H. Zhu *et al.*, "Design principles for compact, backdrivable actuation in partial-assist powered knee orthoses," *IEEE/ASME Transactions on Mechatronics*, vol. 26, no. 6, pp. 3104–3115, Dec. 2021.

[5] T. Zhu, "Design of a Highly Dynamic Humanoid Robot," Ph.D. dissertation, UCLA, 2023.

[6] C. A. Pérez-Díaz *et al.*, "Design and experimental characterisation of a novel quasi-direct drive actuator for highly dynamic robotic applications," in *2024 IEEE International Conference on Robotics and Automation (ICRA)*, May 2024, pp. 183–189.

[7] A. Singh, N. Kashiri, and N. Tsagarakis, "Design of a quasi-direct-drive actuator for dynamic motions," in *The 1st International Electronic Conference on Actuator Technology: Materials, Devices and Applications*, Nov. 2020, p. 11.

[8] S. Yu *et al.*, "Quasi-direct drive actuation for a lightweight hip exoskeleton with high backdrivability and high bandwidth," *IEEE/ASME Transactions on Mechatronics*, vol. 25, no. 4, pp. 1794–1802, Aug. 2020.

[9] T. Yoshida *et al.*, "Experimental evaluation of a quasi-direct-drive actuator with a 3d-printed planetary gear reducer," in *2023 IEEE/SICE International Symposium on System Integration (SII)*, Jan. 2023, pp. 1–6.

[10] K. Urs *et al.*, "Design and characterization of 3d printed, open-source actuators for legged locomotion," in *2022 IEEE/RSJ International Conference on Intelligent Robots and Systems (IROS)*, Oct. 2022, pp. 1957–1964.

[11] W. Roozing and G. Roozing, "3d-printable low-reduction cycloidal gearing for robotics," in *2022 IEEE/RSJ International Conference on Intelligent Robots and Systems (IROS)*, Oct. 2022, pp. 1929–1935.

[12] W. Roozing and G. Roozing, "Experimental comparison of pinwheel and non-pinwheel designs of 3d-printed cycloidal gearing for robotics," in *2024 IEEE International Conference on Robotics and Automation (ICRA)*, May 2024, pp. 7091–7098.

[13] K. Lee, S. Hong, and J.-H. Oh, "Development of a lightweight and high-efficiency compact cycloidal reducer for legged robots," *International Journal of Precision Engineering and Manufacturing*, vol. 21, no. 3, 2019.

[14] A. Zhu *et al.*, *Cycloidal quasi-direct drive actuator designs with learning-based torque estimation for legged robotics*, Oct. 2024. arXiv: 2410.16591[cs].

[15] T. Lenzi, J. Lipsey, and J. W. Sensinger, "The RIC arm—a small anthropomorphic transhumeral prosthesis," *IEEE/ASME Transactions on Mechatronics*, vol. 21, no. 6, pp. 2660–2671, Dec. 2016.

[16] A. Kakogawa *et al.*, "A highly backdrivable robotic arm using low friction and high accuracy cycloidal geared motors: ALFHA," in *2022 IEEE/SICE International Symposium on System Integration (SII)*, Jan. 2022, pp. 428–433.

[17] R. Bezzini *et al.*, "Design and experimental evaluation of multiple 3d-printed reduction gearboxes for wearable exoskeletons," *Robotics*, vol. 13, no. 11, p. 168, Nov. 2024.

[18] H. Satake and N. Takesue, "Comparison of characteristics of cycloidal gear reducer using metal, plastic and 3d printed parts," in *2024 IEEE/SICE International Symposium on System Integration (SII)*, Jan. 2024, pp. 1531–1536.

[19] Z. Cui *et al.*, "Research on tolerance design of 2k-v reducer with beveloid gear considering the effect of anti-backlash," *International Journal of Precision Engineering and Manufacturing*, vol. 25, no. 2, pp. 349–362, Feb. 2024.

[20] G. Sciarra *et al.*, "An innovative low-backlash wolfrom gearbox with beveloid gears for robotic applications," in *New Trends in Mechanism and Machine Science*, vol. 165, Series Title: Mechanisms and Machine Science, 2024, pp. 337–346.

[21] J. Zhang *et al.*, "New type of cycloid planetary reducer for precision transmission," in *Proceedings of the Korean Society of Precision Engineering Conference*, vol. 2009.06a, 2009, pp. 753–754.

[22] Q. Du *et al.*, "A 3k planetary gear train with a flexure-based anti-backlash carrier for collaborative robots," *Mechanism and Machine Theory*, vol. 191, p. 105 495, Jan. 2024.

[23] S. Oba and Y. Fujimoto, "Hybrid 3k compound planetary reduction gearbox with a roller transmission mechanism," *IEEE/ASME Transactions on Mechatronics*, vol. 27, no. 4, pp. 2356–2366, Aug. 2022.

[24] *GO-M8010-6 Motor*, en.

[25] Y.-W. Hwang and C.-F. Hsieh, "Geometric design using hypotrochoid and nonundercutting conditions for an internal cycloidal gear," *Journal of Mechanical Design*, vol. 129, no. 4, pp. 413–420, Apr. 2007.

[26] C.-F. Hsieh, "Dynamics analysis of cycloidal speed reducers with pinwheel and nonpinwheel designs," *Journal of Mechanical Design*, vol. 136, no. 9, p. 091 008, Sep. 2014.

[27] L. C. Hale and A. H. Slocum, "Design of anti-backlash transmissions for precision position control systems," *Precision Engineering*, vol. 16, no. 4, pp. 244–258, Oct. 1994.

[28] Z. Yang *et al.*, "Nonlinear dynamics modeling and analysis of torsional spring-loaded antibacklash gear with time-varying meshing stiffness and friction," *Advances in Mechanical Engineering*, vol. 5, p. 203 438, Jan. 2013.

[29] Y. Kariyama and K. Zushi, "Relationships between lower-limb joint kinetic parameters of sprint running and rebound jump during the support phases," *The Journal of Physical Fitness and Sports Medicine*, vol. 5, no. 2, pp. 187–193, 2016.

[30] J. Volbeda and W. Roozing. "Cost-Effective and Torque-Dense Cycloidal Actuator with Anti-Backlash Mechanisms." (Apr. 2025), [Online]. Available: https://github.com/geez0x1/2025-cycloidal-drive-antibacklash.